2 ABSTRACT

The 'Laser-hybrid Accelerator for Radiobiological Applications', LhARA, is conceived as a novel, ~~uniquely~~ flexible facility dedicated to the study of radiobiology. The technologies demonstrated in LhARA, which have wide application, will be developed to allow particle-beam therapy to be delivered in a ~~completely new~~ regime, combining a variety of ion species in a single treatment fraction and exploiting ultra-high dose rates. LhARA will be a hybrid accelerator system in which laser interactions drive the creation of a large flux of protons or light ions that are captured using a plasma (Gabor) lens and formed into a beam. The laser-driven source allows protons and ions to be captured at energies significantly above those that pertain in conventional facilities, thus evading the current space-charge limit on the instantaneous dose rate that can be delivered. The laser-hybrid approach, therefore, will allow the ~~vast "terra incognita" of the~~ radiobiology that determines the response of tissue to ionising radiation to be studied with protons and light ions using a wide variety of time structures, spectral distributions, and spatial configurations at instantaneous dose rates up to and significantly beyond the ultra-high dose-rate 'FLASH' regime.

It is proposed that LhARA be developed in two stages. In the first stage, a programme of *in vitro* radiobiology will be served with proton beams with energies between 10 MeV and 15 MeV. In stage two, the beam will be accelerated using a fixed-field accelerator (FFA). This will allow experiments to be carried out *in vitro* and *in vivo* with proton beam energies of up to 127 MeV. In addition, ion beams with energies up to 33.4 MeV per nucleon will be available for *in vitro* and *in vivo* experiments. This paper presents the conceptual design for LhARA and the R&D programme by which the LhARA consortium seeks to establish the facility.

23 LAY SUMMARY

It is well established that radiation therapy (RT) is an effective treatment for many types of cancer. Most treatments are delivered by machines that accelerate electrons which are then used to produce a beam of high-energy photons (X-rays) which are directed at a tumour to kill cancer cells. However, healthy tissue anywhere in the path of the photon beam is also irradiated and so can be damaged. Modern X-ray therapy is able to reduce this damage by using several beams at different angles.

Recent years have seen the use of a new type of machine in which protons are accelerated to produce proton beams (rather than photon beams) which are directed at a tumour. These proton beams can be arranged to deposit almost all of their energy in a small volume within a tumour so they cause little damage to healthy tissue; a major advantage over photon beams. But proton machines are large and expensive, so there is a need for the development of proton machines that are smaller, cheaper and more flexible in how they can be used.

The LhARA project is aimed at the development of such proton machines using a new approach based on high powered lasers. Such new machines could also make it easier to deliver the dose in very short high-intensity pulses and as a group of micro-beams—exciting recent research has shown that this brings improved effectiveness in killing cancer cells while sparing healthy tissue. The technology to be proved in LhARA should enable a course of RT to be delivered in days rather than weeks, ~~and should be more effective.~~

Scientifically, there is a need to understand much better the basic processes by which radiation interacts with biological matter to kill cancer cells—the investigation of these processes involves physics as well as biology. Thus the most important aim of LhARA is to pursue this radiobiological

1 INTRODUCTION

Cancer is the second most common cause of death globally [The World Health Organisation (2020)]. In 2018, 18.1 million new cancer cases were diagnosed, 9.6 million people died of cancer-related disease, and 43.8 million people were living with cancer [Bray et al. (2018); Fitzmaurice et al. (2018)]. It is estimated that 26.9 million life-years could be saved in low- and middle-income countries if radiotherapy capacity could be scaled up [Atun et al. (2015)]. Novel techniques incorporated in facilities that are at once robust, automated, efficient, and cost-effective are required to deliver the required scale-up in provision.

Radiation therapy (RT), a cornerstone of cancer treatment, is used in over 50% of cancer patients [Datta et al. (2019)]. The most frequently used types of radiotherapy employ photon or electron beams with MeV-scale energies. Proton and ion beams offer substantial advantages over X-rays because the bulk of the beam energy is deposited in the Bragg peak. This allows dose to be conformed to the tumour while sparing healthy tissue and organs at risk. The benefits of proton and ion-beam therapy (PBT) are widely recognised. PBT today is routinely delivered in fractions of $\sim 2\,\text{Gy}$ per day over several weeks; each fraction being delivered at a rate of $\lesssim 10\,\text{Gy/minute}$ deposited uniformly over the target treatment volume. Exciting evidence of therapeutic benefit has recently been reported when dose is delivered at ultra-high dose-rate, $\gtrsim 40\,\text{Gy/s}$ ("FLASH" RT) [Favaudon et al. (2014); Vozenin et al. (2019)], or provided in multiple micro-beams with diameter less than 1 mm distributed over a grid with inter-beam spacing of $\sim 3\,\text{mm}$ [Prezado et al. (2017)]. However, the radiobiological mechanisms by which the therapeutic benefit is generated are not entirely understood.

LhARA, the Laser-hybrid Accelerator for Radiobiological Applications, is conceived as the new, highly flexible, source of radiation that is required to explore the ~~vast "terra incognita" of~~ the mechanisms by which the biological response to ionising radiation is determined by the physical characteristics of the beam. A high-power pulsed laser will be used to drive the creation of a large flux of protons or light ions which are captured and formed into a beam by strong-focusing plasma lenses. The laser-driven source allows protons and ions to be captured at energies significantly above those that pertain in conventional facilities, thus evading the current space-charge limit on the instantaneous dose rate that can be delivered. The plasma (Gabor) lenses provide the same focusing strength as high-field solenoids at a fraction of the cost. Rapid acceleration will be performed using a fixed-field alternating-gradient accelerator (FFA) thereby preserving the unique flexibility in the time, energy, and spatial structure of the beam afforded by the laser-driven source.

We propose that LhARA be developed in two stages. In the first stage, the laser-driven beam, captured and transported using plasma lenses and bending magnets, will serve a programme of *in vitro* radiobiology with proton beams of energy of up to 15 MeV. In stage two, the beam will be accelerated using an FFA. This will allow experiments to be carried out *in vitro* and *in vivo* with proton-beam energies of up to 127 MeV. Ion beams (including C^{6+}) with energies up to 33.4 MeV per nucleon will also be available.

The laser pulse that initiates the production of protons or ions at LhARA may be triggered at a repetition rate of up to 10 Hz. The time structure of the beam may therefore be varied to interrupt the chemical and biological pathways that determine the biological response to ionising radiation with 10 ns to 40 ns long proton or ion bunches repeated at intervals as small as 100 ms. The technologies chosen to capture, transport, and accelerate the beam in LhARA ~~have been made so that~~ ensure this unique capability is preserved. The LhARA beam may be used to deliver an almost uniform dose distribution over a circular area with a maximum diameter of between 1 cm and 3 cm. Alternatively the beam can be focused to a spot with diameter of $\sim 1\,\text{mm}$.

133 required to treat a particular tumour. Overestimation can lead to risk of damage to healthy tissue, while an
134 underestimate can lead to the tumour not being treated sufficiently for it to be eradicated.

135 Given that the therapeutic effect of RT is largely caused by irreparable damage to the cell's DNA, differences
136 in RBE can also affect the spectrum of DNA damage induced within tumour cells. Larger RBE values,
137 corresponding to higher LET, can cause increases in the frequency and complexity of DNA damage,
138 particularly DNA double-strand breaks (DSB) and complex DNA damage (CDD) where multiple DNA
139 lesions are induced in close proximity [Vitti and Parsons (2019); Carter et al. (2018)]. These DNA lesions
140 are a major contributor to radiation-induced cell death as they represent a significant barrier to the cellular
141 DNA-repair machinery, including base excision repair for DNA-base damage and single-strand breaks,
142 while non-homologous end-joining and homologous recombination are utilised to repair DSBs [Vitti and
143 Parsons (2019)]. However, a number of other biological factors contribute to varying RBE in specific
144 tumours, including the intrinsic radiosensitivity of the tissue, the level of oxygenation (hypoxia), the growth
145 and repopulation characteristics, and the associated tumour micro-environment. Consequently, there is still
146 significant uncertainty in the precise radiobiological mechanisms that arise and how these mechanisms
147 are affected by PBT, which is necessary for optimal patient-treatment strategies to be devised. Detailed
148 systematic studies of the biophysical effects of the interaction of protons and ions, under different physical
149 conditions, with different tissue types will provide important information on RBE variation and could
150 enable enhanced treatment-planning algorithms to be devised. In addition, studies examining the impact of
151 combination therapies with PBT (e.g. targeting the DNA damage response, hypoxia signalling mechanisms
152 and also the tumour micro-environment) are currently sparse; performing these studies will therefore
153 provide input vital to the development of future personalised patient-therapy strategies using PBT.

The case for novel beams for radiobiology
155 PBT delivery to date has been restricted to a small number of beam characteristics. In a typical treatment
156 regimen the therapeutic dose is provided in a series of daily sessions delivered over a period of several
157 weeks. Each session consisting of a single fraction of $\sim$2 Gy delivered at a rate of $\lesssim$ 5 Gy/minute. Recent
158 reports provide exciting evidence of therapeutic benefit when the dose is delivered at ultra-high dose
159 rate ($>$ 40 Gy/s) "FLASH" RT [Favaudon et al. (2014); Vozenin et al. (2019)]. These studies indicate
160 significantly reduced lung fibrosis in mice, skin toxicity in mini-pigs, and reduced side-effects in cats with
161 nasal squamous-cell carcinoma, which is currently thought to be mediated via local oxygen depletion. In
162 fact, the first patient with CD30+ T-cell cutaneous lymphoma has been shown to be safely treated with
163 electrons delivered at FLASH dose rates. In addition, therapeutic benefit has been demonstrated with
164 the use of multiple micro-beams with diameter of less than 1 mm distributed over a grid with inter-beam
165 spacing of 3 mm [Prezado et al. (2017)]. However, there is still significant uncertainty regarding the
166 thresholds and the radiobiological mechanisms by which therapeutic benefit is generated in FLASH and
167 micro-beam therapy, which require extensive further study both *in vitro* and in appropriate *in vivo* models.

168 LhARA is designed to be a highly flexible source delivering the temporal, spectral, and spatial beam
169 structures that are required to elucidate the mechanisms by which the biological response to ionising
170 radiation is determined by the physical characteristics of the beam, including FLASH and micro-beam
171 effects. These comprehensive studies are not currently possible at clinical RT facilities. Thus the LhARA
172 facility will provide greater accessibility to stable ion beams, enable different temporal fractionation
173 schemes, and deliver reliable and reproducible biological data with fewer constraints than at current clinical
174 centres. The availability of several ion beams (from protons to heavier ions) within the same facility will
175 provide further flexibility and the ability to perform direct radiobiological comparisons of the effect of
176 different charged particles. In addition, LhARA will enable exhaustive evaluations of RBE using more
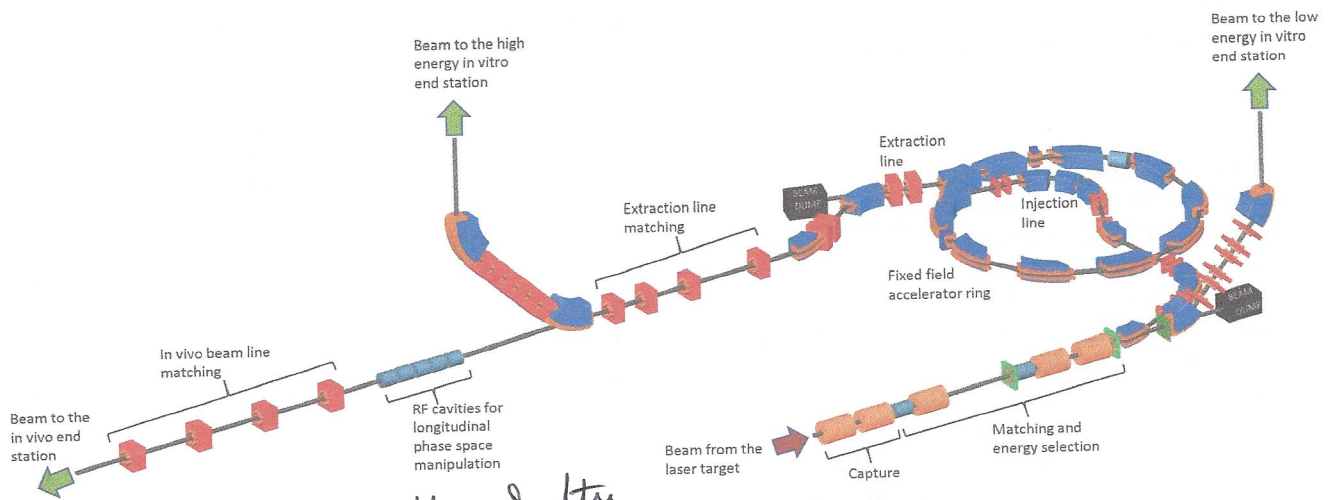
Figure 1. Schematic diagram of the LhARA beam lines. The particle flux from the laser-driven source is shown by the red arrow. The 'Capture' section is followed by the 'Matching and energy selection' section. The beam is then directed either into the 90° bend that takes it to the low-energy *in vitro* end station, towards the FFA injection line, or to the low-energy beam dump. Post acceleration is performed using the FFA on extraction from which the beam is directed either to the high-energy *in vitro* end station, the *in vivo* end station, or the high-energy beam dump. Gabor lenses are shown as the orange cylinders, RF cavities as grey cylinders, quadrupole magnets as red squares, octopole magnets as green discs, and dipole magnets are shown in blue. The beam-line elements are discussed in section 3.

219   • The demonstration in operation of technologies that will allow PBT to be delivered in completely new
220   regions.
221

3   THE LHARA FACILITY

222   The LhARA facility, shown schematically in figure 1, has been designed to serve two end stations for
223   *in vitro* radiobiology and one end station for *in vivo* studies. The principle components of the LhARA
224   accelerator are: the laser-driven proton and ion source; the matching and energy selection section; beam
225   delivery to the low-energy *in vitro* end station; the low-energy abort line; the injection line for the fixed-
226   field alternating-gradient accelerator (FFA); the FFA; the extraction line; the high-energy abort line; beam
227   delivery to the high-energy *in vitro* end station; and the transfer line to the *in vivo* end station. Proton beams
228   with energies of between 12 MeV and 15 MeV will be delivered directly from the laser-driven source to
229   the low-energy *in vitro* end station via a transfer line. The high-energy *in vitro* end station and the *in vivo*
230   end station will be served by proton beams with energy between 15 MeV and 127 MeV and by ion beams,
231   including C^{6+} with energies up to 33.4 MeV/u. This configuration makes it natural to propose that LhARA
232   be constructed in two stages; Stage 1 providing beam to the low-energy *in vitro* end station and Stage 2
233   delivering the full functionality of the facility. The development of LhARA Stage 1 will include machine
234   performance and optimisation studies designed to allow *in vitro* experiments to begin as soon as possible.

235   The design parameters for the various components of LhARA are given in tables 1 and 2. The design of
236   the LhARA facility is described in the sections that follow.
237

3.1   Laser-driven proton and ion source

239   Laser-driven ions have been posited as a source for radiobiological studies for a number of years [Kraft
240   et al. (2010); Yogo et al. (2011); Bin et al. (2012)]. Until now, the achievable ion energies, energy

Table 2. Design parameters of the components of the LhARA facility. The parameter table is provided in a number of sections. This section contains parameters for the Stage 2 beam transport and the *in vitro* and *in vivo* end stations.

Parameter	Value or range	Unit
Stage 2 beam transport: FFA, transfer line, beam delivery to high-energy end stations		
Number of bending magnets in the injection line	7	
Number of quadrupoles in the injection line	10	
FFA: Machine type	single spiral scaling FFA	
FFA: Extraction energy	15–127	MeV
FFA: Number of cells	10	
FFA: Orbit R_{min}	2.92	m
FFA: Orbit R_{max}	3.48	m
FFA: Orbit excursion	0.56	m
FFA: External R	4	m
FFA: Number of RF cavities	2	
FFA: RF frequency	1.46–6.48	MHz
FFA: harmonic number	1, 2 or 4	
FFA: RF voltage (for 2 cavities)	4	kV
FFA: spiral angle	48.7	Degrees
FFA: Max B field	1.4	T
FFA: k	5.33	
FFA: Magnet packing factor	0.34	
FFA: Magnet opening angle	12.24	degrees
FFA: Magnet gap	0.047	m
FFA: Ring tune (x,y)	(2.83,1.22)	
FFA: γ_T	2.516	
FFA: Number of kickers	2	
FFA: Number of septa	2	
Number of bending magnets in the extraction line	2	
Number of quadrupoles in the extraction line	8	
Vertical arc bending angle	90	Degrees
Number of bending magnets in the vertical arc	2	
Number of quadrupoles in the vertical arc	6	
Number of cavities for longitudinal phase space manipulation	5	
Number of quadrupoles in the in vivo beam line	4	
***In vitro* biological end stations**		
Maximum input beam diameter	1-3	cm
Beam energy spread (full width)	Low-energy end station: ≤ 4	%
	High-energy end station: ≤ 1	%
Input beam uniformity	< 5	%
Scintillating fibre layer thickness	0.25	mm
Air gap length	5	mm
Cell culture plate thickness	1.3	mm
Cell layer thickness	0.03	mm
Number of end stations	2	
***In vivo* biological end station**		
Maximum input beam diameter	1-3	cm
Beam energy spread (full width)	≤ 1	%
Input beam uniformity	< 5	%
Beam options	Spot-scanning, passive scattering, micro-beam	

301 for LhARA are discussed in section 3.5.

302

3.2 Proton and ion capture

304 The use of an electron cloud as a focusing element for charged-particle beams was first proposed by
305 Gabor in 1947 [Gabor (1947)]. Gabor noted that a cloud of electrons uniformly distributed about the axis
306 of a cylindrical vessel would produce an ideal focusing force on a beam of positively charged particles. The
307 focal length of such a lens scales with the energy of the incoming particle beam, allowing such lenses to
308 provide strong focussing of high-energy beams. Confinement conditions in the radial and axial directions
309 can be determined [Pozimski and Aslaninejad (2013)]. In the radial direction, where there is magnetic
310 confinement and Brillouin flow, the number density of electrons, n_e, that can be contained is given by:

$$n_e = \frac{\epsilon_0 B^2}{2m_e} \; ; \tag{1}$$

311 where B is the magnetic field, m_e the mass of the electron, and ϵ_0 the permittivity of free space. In the
312 longitudinal direction there is electrostatic confinement for which n_e is given by:

$$n_e = \frac{4\epsilon_0 V_A}{eR^2} \; ; \tag{2}$$

313 where e the magnitude of the charge on the electron and R is the radius of the cylindrical anode which
314 is held at the positive potential V_A. For the electron densities of interest for LhARA the required anode
315 voltage is of the order of 50 kV.

316 In the thin lens approximation, the focal length, f, of a Gabor lens can be expressed in terms of the
317 magnetic field and the particle velocity, v_p [Reiser (1989)]:

$$\frac{1}{f} = \frac{e^2 B^2}{4m_e m_p v_p^2} l \; ; \tag{3}$$

318 where m_p is the mass of the particles in the beam. The focal length of the Gabor lens is therefore
319 proportional to the kinetic energy or, equivalently, the square of the momentum, of the incoming beam. By
320 comparison, the focal length for a solenoid is proportional to the square of the momentum and that of a
321 quadrupole is proportional to momentum. At the particle energies relevant to LhARA the Gabor lens, or
322 the solenoid, is therefore preferred. The focal length f a Gabor lens ...

323 An expression for the focal length as a function of electron number density can be derived by substituting
324 equation (1) into equation (3) to give:

$$\frac{1}{f} = \frac{e^2 n_e}{4\epsilon_0 U} l \; ; \tag{4}$$

325 where $U = \frac{1}{2} m_p v_p^2$ is the kinetic energy of the particle beam. The focal length of the Gabor lens is inversely
326 proportional to the number density of electrons trapped in the cloud. The focal lengths desired to capture
327 the proton and ion beams at LhARA have been chosen such that the required electron number densities are
328 conservative and lie within the range covered in published experiments.

329 For a given focal length, the magnetic field required in the Gabor lens is reduced compared to that of a
330 solenoid that would give equivalent focusing. In the non-relativistic approximation the relationship between
331 the magnetic field in the Gabor lens, B_{GBL}, and the equivalent solenoid, B_{sol}, is given by [Pozimski and

356 LhARA beam. In addition, the initial investigation will include the design of an electron beam to fill the
357 lens. This last objective will enable the second part of the experimental project; the operation of the Gabor
358 lens in short pulses. It is attractive to match the timing of the establishment of the electron cloud within the
359 Gabor lens to that of the beam and thereby limit instability growth. (The research project is time limited
360 such that, should it not prove possible to produce a suitable Gabor lens, there will remain time sufficient to
361 procure conventional solenoids in their place.)

362

3.3 Beam transport and delivery to the low-energy *in vitro* end station

364 Beam-transport from the laser-driven ion source and delivery to the low-energy *in vitro* end station is
365 required to deliver a uniform dose distribution at the cell layer. Beam losses must be minimised for radiation
366 safety and to maximise the dose that can be delivered in a single shot. The transport line has been designed
367 to minimise regions in which the beam is brought to a focus to reduce the impact of space-charge forces on
368 the beam phase-space. An optical solution was initially developed using Beamoptics [Autin et al. (1998)]
369 and MADX [Grote and Schmidt (2003)]. Accurate estimation of the performance of the beam line requires
370 the inclusion of space-charge forces and particle-matter interactions. Therefore, performance estimation
371 was performed using Monte Carlo particle-tracking from the ion source to the end station. BDSIM [Nevay
372 et al. (2020)], which is based on the Geant4 toolkit was used for the simulation of energy deposition arising
373 from beam interactions with the material in the accelerator and the end station. GPT [De Loos and Van der
374 Geer (1996)] was used for evaluating the full 3D impact of space-charge.

375 An idealised Gaussian beam was generated with a spot size of 4 μm FWHM, an angular divergence of
376 50 mrad, 35 fs FWHM bunch length, and an energy spread of 1×10^{-6} MeV. The maximum estimated
377 bunch charge is 1×10^9 protons. The presence of a substantial electron flux produced from the laser target
378 compensates the high proton charge density in the vicinity of the ion-production point. Therefore, the first
379 5 cm of beam propagation was simulated without space-charge. Beyond this, the proton beam will have
380 separated from the lower energy electrons sufficiently for space-charge to become a prominent effect and
381 cause an emittance growth. Therefore, a further 5 cm drift was simulated including space-charge forces. At
382 a distance of 10 cm from the ion source the beam is at the exit of the laser-target vessel. The kinematic
383 distributions of ions in the beam were stored at this point and passed to the relevant BDSIM and GPT
384 simulations of the downstream beam line.

385 The beam line, shown schematically in figure 3, is composed of five sections: beam capture; matching
386 and energy selection; beam shaping; vertical arc matching; and an abort line. The capture section uses two
387 Gabor lenses to minimise the transverse momentum of particles in the beam. Beyond the capture section,
388 an RF cavity permits control of the bunch length and manipulation of the longitudinal phase-space. A third
389 Gabor lens then focuses the bunch to a small spot size after which a second RF cavity is located to provide
390 further longitudinal phase-space manipulation. Two further Gabor lenses bring the beam parallel once more
391 in preparation for the vertical 90° arc. All Gabor lenses have an inner radius of 3.65 cm and an effective
392 length of 0.857 m. All lenses operate below the maximum cathode voltage of 65 kV.

393 A parallel beam emerges from the final Gabor lens, providing significant flexibility for the inclusion of
394 beam shaping and extraction systems. Beam uniformity will be achieved using octupole magnets to provide
395 third-order focusing to perturb the first-order focusing from the Gabor lenses. Such schemes have been
396 demonstrated in a number of facilities [Tsoupas et al. (1991); Urakabe et al. (1999); Amin et al. (2018)].
397 A suitable position for the first octupole was identified to be after the final Gabor lens where the beam is
398 large; its effect on the beam is expected to be significant. Octupoles were only modelled in BDSIM as GPT
399 does not have a standard component with an octupolar field. The typical rectangular transverse distribution
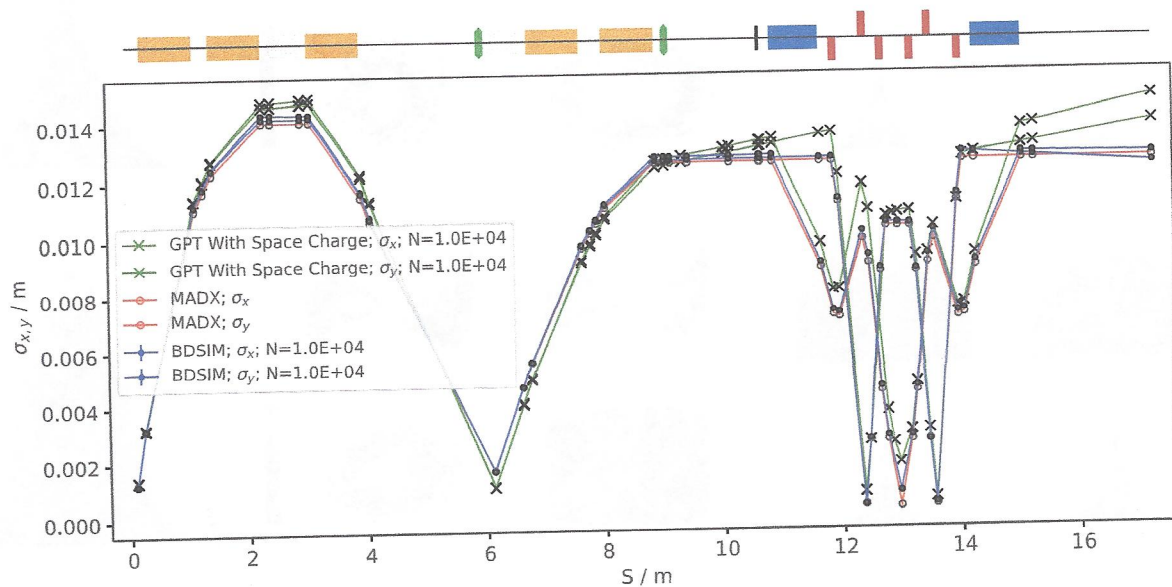
Figure 4. Horizontal (solid lines) and vertical (dashed lines) beam sizes through the *in vitro* beam transport, simulated with space-charge in GPT (green), and without space-charge in MADX (red) and BDSIM (blue).

424 underestimated. Similar bunch dimensions are achieved in the vertical arc, however, quadrupolar focusing
425 is confined to a single plane mitigating further emittance growth. Further tuning of the Gabor lens voltages
426 in the capture section may compensate space-charge effects, reducing the non-zero transverse momentum
427 seen entering the vertical arc.

428   To investigate beam uniformity, BDSIM simulations with and without octupoles and collimation for beam
429 shaping were conducted. Both octupoles were arbitrarily set to a strength of $K3 = 6000$ with a magnetic
430 length of 0.1 m and pole-tip radius of 5 cm, which, for a 15 MeV beam corresponds to pole-tip field of
431 0.42 T. A 2 cm thick iron collimator with a 40 mm diameter aperture was positioned 1.5 m downstream
432 of the octupole. Figure 5 shows the beam phase-space and particle distributions at the end station for the
433 transverse and longitudinal axes with and without beam shaping. Without octupoles the spatial profile
434 is Gaussian, as expected, however, beam uniformity is improved with octupoles and collimation. The
435 total beam width is 3.58 cm horizontally and 3.46 cm vertically, which is sufficient to irradiate one well
436 in a six-well cell-culture plate. Further optimisation is required to improve uniformity whilst optimising
437 beam-line transmission, which is approximately 70% for the results presented in figure 5. An aberration
438 can be seen in both transverse planes with and without beam shaping; this effect originates upstream of
439 the octupoles in the solenoids, and persists through to the end station. These aberrations are a concern,
440 however, future simulation efforts will replace the solenoids with a full electromagnetic simulation of the
441 Gabor lens. This change is likely to change the aberrations. The non-Gaussian energy distribution without
442 beam shaping is a result of space-charge forces at the ion source; the distribution persists to the end station
443 as no components which affect the longitudinal phase space were simulated. The Gaussian distribution
444 seen with beam shaping is due to collimation.

445   The proposed design is capable of delivering beams of the desired size to the *in vitro* end station. Space-
446 charge effects impact the beam-transport performance but it is believed that this can be mitigated with
447 minor adjustments to the Gabor lenses in the capture section. Initial studies indicate that a uniform beam

469 ions delivered by the laser-driven source. FFAs have many advantages for both medical and radiobiological
470 applications such as: the capability to deliver high and variable dose; rapid cycling with repetition rates
471 ranging from 10 Hz to 100 Hz or beyond; and the ability to deliver various beam energies without the use
472 of energy degraders. An FFA is relatively compact due to the use of combined function magnets, which
473 lowers the overall cost compared to conventional accelerators capable of delivering beams at a variety of
474 energies such as synchrotrons. Extraction can be both simple and efficient and it is possible for multiple
475 extraction ports to be provided. Furthermore, FFAs can accelerate multiple ion species, which is very
476 important for radiobiological experiments and typically very difficult to achieve with cyclotrons.

477 A typical FFA is able to increase the beam momentum by a factor of three, though a greater factor may
478 be achieved. For LhARA, this translates to a maximum proton-beam energy of 127 MeV from an injected
479 beam of 15 MeV. For carbon ions (C^{6+}) with the same rigidity, a maximum energy of approximately
480 33.4 MeV/u can be produced.

481 The energy at injection into the FFA determines the beam energy at extraction. The injection energy will
482 be changed by varying the focusing strengths in the Stage 1 beam line from the capture section through to
483 the extraction line and the FFA ring. This will allow the appropriate energy slice from the broad energy
484 spectrum produced at the laser-driven source to be captured and transported to the FFA. The FFA will then
485 accelerate the beam, acting as a three-fold momentum multiplier. This scheme simplifies the injection and
486 extraction systems since their geometry and location can be kept constant.

487 A second, 'high-energy', *in vitro* end station will be served by proton beams with a kinetic energy in the
488 range 15–127 MeV and carbon-ion beams with energies up to 33.4 MeV/u. The extraction line from the
489 FFA leads to a 90° vertical arc to send the beam to the high-energy *in vitro* end station. If the first dipole
490 of the arc is not energised, the beam will be sent to the *in vivo* end station. The extraction line of the FFA
491 includes a switching dipole that will send the beam to the high-energy-beam dump if it is not energised.
492 The detailed design of the high-energy abort line, taking into account the requirement that stray radiation
493 does not enter the end stations, will be performed as part of the LhARA R&D programme.

494
495 3.4.1 Injection line

496 The settings of the Stage 1 beam line need to be adjusted to reduce the Twiss β function propagating
497 through the injection line to allow the beam to be injected into the FFA ring. The optical parameters in the
498 Stage 1 beam line after adjustment are shown in figure 6. The beam is diverted by a switching dipole into
499 the injection line which transports the beam to the injection septum magnet. The injection line matches
500 the Twiss β functions in both transverse planes and the dispersion of the beam to the values dictated by
501 the periodic conditions in the FFA cell (figure 6). The presence of dispersion in the injection line allows a
502 collimator to be installed for momentum selection before injection. The beam is injected from the inside of
503 the ring, which requires the injection line to cross one of the straight sections between the FFA magnets,
504 see figure 7.

505
506 3.4.2 FFA ring

507 The magnetic field, B_y, in the median plane of a scaling spiral FFA is given by [Krest et al. (1956); Symon
508 et al. (1956); Fourrier et al. (2008)]:

$$B_y = B_0 \left[\frac{R}{R_0} \right]^k F \left(\theta - \ln \left[\frac{R}{R_0} \right] \tan \zeta \right) ; \tag{6}$$
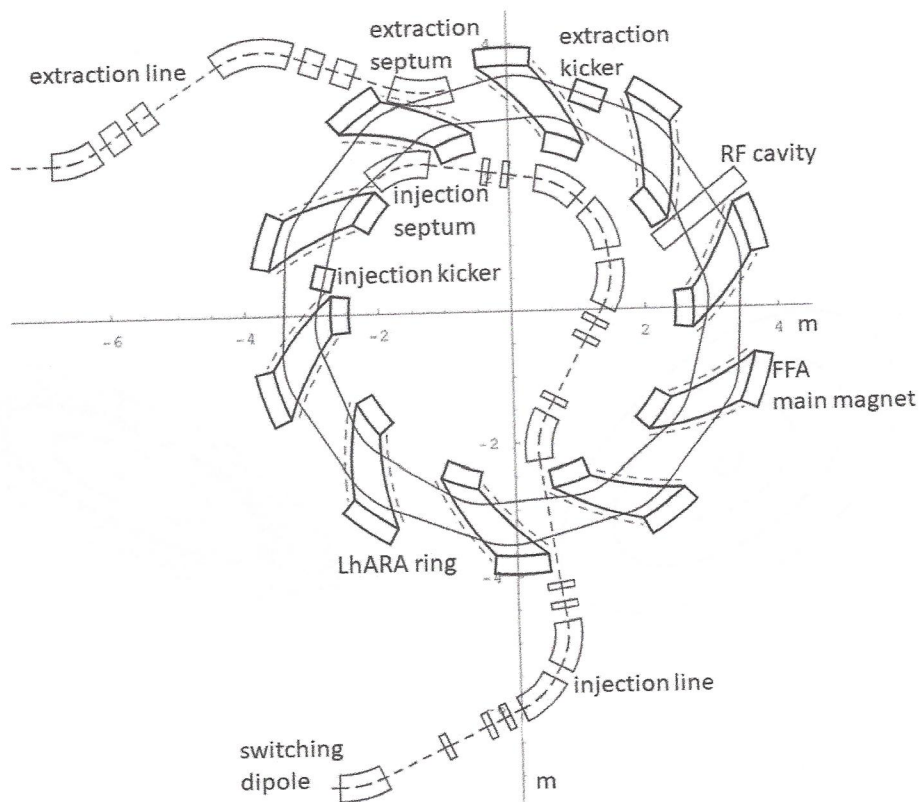
Figure 7. The layout of the injection line from the switching dipole to the injection septum together with the FFA ring, some of its subsystems and the first part of the extraction line.

Table 3. Summary of the main parameters for the proton beam at the injection to the FFA ring. These parameters correspond to the nominal (maximum) acceleration mode of operation.

Parameter	Unit	Value
Beam energy	MeV	15
Total relative energy spread	%	±2
Nominal physical RMS emittance (both planes)	π m rad	4.1×10^{-7}
Incoherent space charge tune shift		-0.8
Bunching factor		0.023
Total bunch length	ns	8.1
Bunch intensity		10^9

[handwritten margin note: inconsistent fonts?]

529 The specifications of the injection system are dictated by the parameters of the beam at injection, which are
530 summarised for the nominal proton beam in table 3. The beam at injection has a relatively small emittance
531 and short bunch length, which limits the intensity accepted by the ring due to the space-charge effect. An
532 intensity of approximately 10^9 protons will be accepted by the ring assuming the nominal beam parameters.
533 Space-charge effects will be severe immediately after injection, but will quickly be reduced due to the
534 debunching of the beam. Fast extraction of the beam over the full aperture will be performed using a kicker
535 magnet followed by a magnetic septum installed in a consecutive lattice cell close to the extraction orbit.

536   Acceleration of the beam to 127 MeV will be done using an RF system operating at harmonic number
537 $h = 1$ with an RF frequency range from 2.89 MHz to 6.48 MHz. The RF voltage required for 10 Hz
538 operation is 0.5 kV. However, at such a low voltage the energy acceptance at injection will be limited to

Table 4. Beam emittance values and target β values for different beam sizes for 40 MeV and 127 MeV beams. The beam size is taken to be four times the sigma of the transverse beam distribution.

	40 MeV protons (Nominal)	127 MeV protons (Nominal)	127 MeV protons (Pessimistic)
RMS Emittance (ϵ_x, ϵ_y) [π mm mrad]	0.137	0.137	1.37
β [m] for a 1 mm spot size	0.46	0.46	0.039
β [m] for a 10 mm spot size	46	46	4.5
β [m] for a 30 mm spot size	410	410	40

3.4.3 Extraction Line

Substantial margins in the beam parameters were assumed in the design of the extraction line from the FFA due to uncertainties in the beam distributions originating from: the Stage 1 beam transport; the FFA injection line; and potential distortions introduced by the presence of space-charge effects during acceleration in the ring. Therefore, the beam emittance was allowed, pessimistically, to be as large as a factor of ten greater than in the nominal value, which was derived assuming that the normalised emittance is conserved from the source, through the Stage 1 beam line, and in the FFA ring. In the nominal case, the physical emittance of the beam is affected by adiabatic damping only. Substantial flexibility in the optics of the extraction line is required, as the extraction line must accommodate a wide spectrum of beam conditions to serve the *in vitro* and *in vivo* end-stations.

Detailed studies were carried out for proton beams with kinetic energies of 40 MeV and 127 MeV. Table 4 gives the Twiss β values for different beam sizes for the 40 MeV and 127 MeV proton-beam scenarios assuming a Gaussian beam distribution. The optics and geometric acceptance of the system is approximately the same for the 40 MeV and 127 MeV beams. This justified the working hypothesis that beam emittance is approximately the same for both beam energies. This assumption will be revised as soon as space-charge simulations for the entire system are available.

The first two dipoles and four quadrupoles of the extraction line bend the beam coming from the extraction septum of the FFA such that it is parallel to the low-energy beam line while ensuring that dispersion is closed. Closing the dispersion is critical as off-momentum particles will follow trajectories different to those followed by particles with the design momentum and therefore impact the size and shape of the beam downstream. The second part of the extraction line consists of four quadrupoles which transport the beam either to the first dipole of the vertical arc that serves the high-energy *in vitro* end station or to the *in vivo* end-station if this dipole is not energised. These quadrupoles provide the flexibility required to produce the different beam sizes for the *in vitro* end station as specified in table 4.

3.4.4 High-energy *in vitro* beam line

The high-energy *in vitro* beam line transports the beam from the exit of the extraction line and delivers it to the high-energy *in vitro* end station. The 90° vertical bend is a scaled version of the low-energy vertical arc, following the same design principles, and also consists of two bending dipole magnets and six quadrupole magnets. To accommodate the higher beam energies, the lengths of the magnets were scaled in order to ensure that peak magnetic fields were below the saturation limits of normal conducting magnets. The bending dipole magnet lengths were increased to 1.2 m each and the quadrupole lengths were tripled to 0.3 m each. The overall length of the arc then becomes 6 m, compared to 4.6 m for the low energy *in vitro* arc. This difference in arc length means the high-energy *in vitro* arc finishes about 0.9 m higher than the low-energy one. This difference can easily be accommodated by adjusting the final drift lengths.
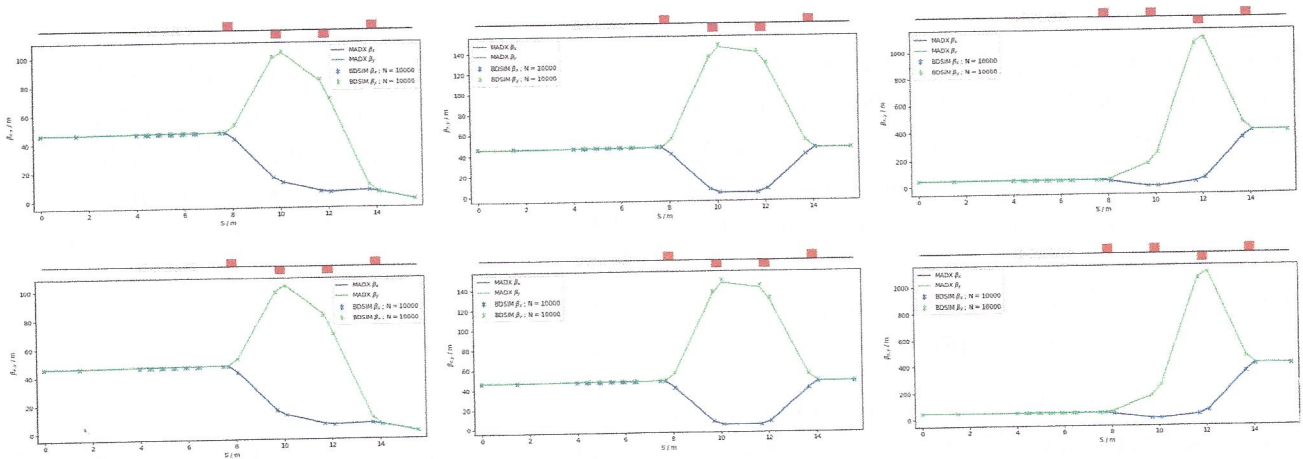
Figure 10. MAD-X and BDSIM simulations of the *in vivo* beam line for a 40 MeV proton beam (top row) and a nominal 127 MeV proton beam (bottom row) with quadrupoles matched to $\beta_{x,y} = 0.46$ m (left), $\beta_{x,y} = 46$ m (middle) and $\beta_{x,y} = 410$ m (right) for 10^4 particles.

624 facilities. Instrumentation for the detection of secondary particles arising from the interaction of the beam
625 with tissue is not discussed here but is an important area that will be studied in the future.
626

627 ### 3.5.1 SciWire
628 For the Stage 1 beam, the maximum proton energy is 15 MeV. Shot-to-shot characterisation of the beam is
629 essential and requires the use of a very thin detector with a fast response. The SciWire [Kurup (2019)] is
630 being developed to provide energy and intensity profile measurements for low-energy ion beams. A single
631 SciWire plane consists of two layers of 250 μm square-section scintillating fibres, with the fibre directions
632 in the two layers orthogonal to each other. A series of back-to-back planes provides a homogeneous volume
633 of scintillator. If there are enough planes to stop the beam, the depth of penetration will allow the beam
634 energy to be inferred. This is obviously a destructive measurement so it is envisaged that this type of
635 measurement would only be used when experiments are not running. A single plane, however, can be used
636 for 2D beam-profile measurements at the same time that beam is delivered for experiments. Detection of
637 the light from SciWire fibres may be by CMOS camera, or using photodiodes. If the instrumentation is
638 sufficiently fast, the SciWire can be used to derive feedback signals for beam tuning.
639

640 ### 3.5.2 SmartPhantom
641 To study in real time the dose profile of Stage 2 beams, the SmartPhantom [Barber (2018)] is being
642 developed. This is a water-filled phantom, which is instrumented with planes of scintillating fibres, by
643 which to infer the dose distribution with distance. The detection elements of the SmartPhantom are 250 μm
644 diameter, round scintillating fibres. Each fibre station consists of two planes of fibres, in which the fibre
645 directions are orthogonal. Five fibre stations are arranged in the phantom in front of the cell-culture flask.
646 The fibres may be coupled to photodiodes, or a CMOS camera. Simulations in GEANT4 are being used to
647 develop analysis techniques by which to predict the position of the Bragg peak shot-by-shot. The beam
648 profile and dose delivered can then be calculated in real time. The key emphasis is to be able to derive these
649 parameters from shot-by-shot data, and not purely from simulations.
650

694 hypoxia chamber (for long-term hypoxia studies), a robotic workstation (handling and processing of large
695 sample numbers, assisting in high-throughput screening experiments), and an ultra-pure-water delivery
696 system. These facilities will enable a myriad of biological end-points to be investigated in both normal-
697 and tumour-cell models not only from routine clonogenic survival and growth assays, but will expand
698 significantly on more complex end-points (e.g. inflammation, angiogenesis, senescence and autophagy)
699 as these experiments are difficult to perform at current clinical research beams due to limited time and
700 facilities. (omit last sentence?)

701   The *in vivo* end-station will be served with high-energy proton and carbon ions capable of penetrating
702 deeper into tissues allowing the irradiation of whole animals. The ability to perform *in vivo* pre-clinical
703 studies is vital for the future effective translation of the research into human cancer patients where optimum
704 treatment strategies and the reduction of side-effects are crucial. The *in vivo* end-station will allow the
705 irradiation of a number of small-animal models (e.g. xenograft mouse and rat models) which can further
706 promote an examination of particular ions on the appropriate biological end-points (e.g. tumour growth
707 and normal tissue responses). The end-station will contain a small-animal handling area which will allow
708 for the anaesthetisation of animals prior to irradiation. To enable the irradiation of small target volumes
709 with a high level of precision and accuracy, an image guidance system (e.g. computed tomography) will be
710 available. The animals will subsequently be placed in temperature-controlled holder tubes enabling the
711 correct positioning of the relevant irradiation area in front of the beam line. The beam size is sufficient to
712 give flexibility in the different irradiation conditions, in particular through passive scattering, pencil-beam
713 scanning, and micro-beam irradiation, to be investigated at both conventional and FLASH dose rates. It is
714 envisaged that the animals will be taken off-site post-irradiation to a nearby animal-holding facility for a
715 follow-up period where biological measurements will be conducted.

3.7   Infrastructure and integration

718 The LhARA facility will encompass two floors of roughly 42 m in length and 18 m wide. The ground floor
719 will contain the laser, accelerator, and *in vivo* end station while the first floor will house the laboratory area
720 and the two *in vitro* end stations. The entire facility will require radiation protection in the form of concrete
721 shielding, which will delineate the facility into three principal areas: a radiation-controlled-access area, a
722 laser controlled-access area, and a laboratory limited-access area.

723   It is envisaged that LhARA will be built at a national Laboratory or equivalent research institute which
724 has an established safety-management system and culture in place. At STFC, a comprehensive set of Safety
725 Codes has been developed to cover the hazards associated with working in such an environment. STFC
726 Safety Codes applicable to LhARA include: risk management, construction, biological safety, working
727 with lasers, working with time-varying electro-magnetic fields, management of ionising radiation, and
728 electrical safety. In practice at STFC, these codes are backed-up by the knowledge, skills and experience
729 of staff, and by appointed responsible persons such as Radiation Protection Advisors, Laser Responsible
730 Officers, and Authorising Engineers. In addition, STFC operates many facilities that encompass the same
731 hazards as LhARA, which, for lasers, include the Gemini Target Areas 2 and 3 [STFC (2019a)] as well as
732 the new EPAC Extreme Photonics Application Centre [STFC (2019b)] and for accelerators include FETS the
733 Front End Test Stand [Letchford et al. (2015)], and the ISIS Neutron and Muon Source [STFC (2019c)].
734 Safety systems and equipment will be required for LhARA, which will include Class II biological safety
735 cabinets for contaminant-free cell culture for *in vitro* radiobiological experiments.
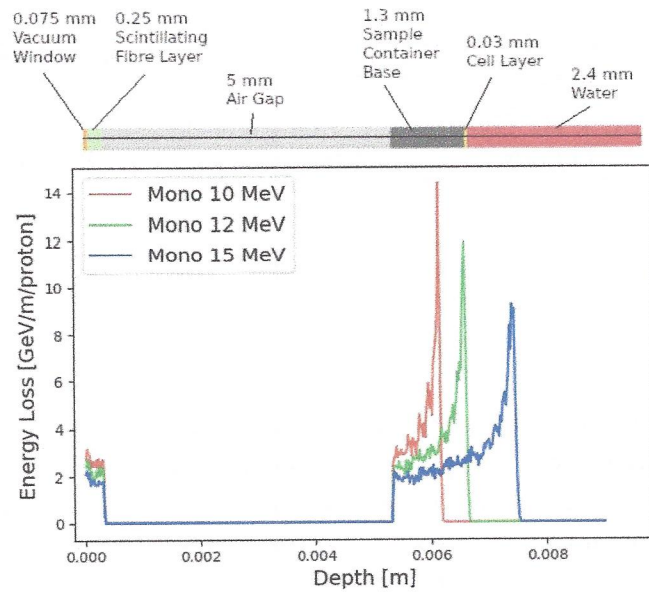
Figure 11. Energy loss as a function of depth in the low-energy *in vitro* end station for three mono-energetic proton energies: 10 MeV; 12 MeV; and 15 MeV. Each beam was simulated using 10^4 particles at the start of the simulated end station. The material through which the beam passes is indicated above the figure. The entrance window is plotted at a Depth value of 0 m. The beam deposits energy in the beam window and the layer of scintillating fibre before passing through the air and entering the sample container.

778   This gives an instantaneous dose rate of 1.8×10^9 Gy/s and an average dose rate of 128 Gy/s assuming the
779   same bunch length and repetition rate as for the 12 MeV case.

780   For the high-energy *in vitro* end station, a different setup was used for high-energy proton beams. A
781   similar design to the low-energy end station was used but with the air gap increased from 5 mm to 5 cm and
782   a water phantom was placed at the end of the air gap instead of a cell culture plate. The water phantom
783   used in the simulation was based upon the PTC T41023 water phantom [PTW (2009)]. In addition, the
784   smaller minimum design beam size of 1 mm was used. A single shot of 10^9 protons at 127 MeV deposits
785   6.9×10^{-4} J in the chamber at the pristine Bragg peak depth corresponding to a dose of 15.6 Gy, an
786   instantaneous dose rate of 3.8×10^8 Gy/s and an average dose rate of 156 Gy/s. The end-station design
787   assumed for a 33.4 MeV/u carbon beam was the same as that used for the low-energy *in vitro* end station
788   due to the limited range in water of the carbon beam. The intensity of the beam is a factor of 12 less than
789   for protons in order to preserve the same strength of the space-charge effect at injection into the FFA with
790   the same beam parameters, as the incoherent space charge tune shift is proportional to q^2/A and inversely
791   proportional to $\beta^2 \gamma^3$, where q corresponds to the particle charge, A its mass number and β, γ its relativistic
792   parameters. A single pulse of 8.3×10^7 ions, deposits 3.2×10^{-3} J at the depth of the pristine Bragg peak,
793   leading to an instantaneous dose rate of 9.7×10^8 Gy/s and a maximum average dose rate of 730 Gy/s.

794   The expected maximum dose rates are summarised in table 5. The instantaneous dose rates depend on
795   the bunch length which differs depending on the energies. For the low-energy *in vitro* line, a 7 ns bunch
796   length is assumed here for all energies. While for the higher energies, a 127 MeV proton beam is delivered
797   with a bunch length of 41.5 ns, and a bunch length of 75.2 ns for a 33.4 MeV/u carbon beam. The same
798   repetition rate of 10 Hz was used for all energies. The minimum beam size at the start of the end station for
799   the 12 MeV and 15 MeV proton-beam simulations was 1 cm. A 1 mm beam size was used for the 127 MeV